Optics Letters

Add–drop filter with complex waveguide Bragg grating and multimode interferometer operating on arbitrarily spaced channels

Shengjie Xie,[1] Jiahao Zhan,[1] Yiwen Hu,[1] Yang Zhang,[1] Sylvain Veilleux,[2] Joss Bland-Hawthorn,[3] and Mario Dagenais[1,*]

[1]Department of Electrical and Computer Engineering, University of Maryland, College Park, Maryland 20742, USA
[2]Department of Astronomy, University of Maryland, College Park, Maryland 20742, USA
[3]Sydney Institute for Astronomy and Sydney Astrophotonic Instrumentation Labs, School of Physics, University of Sydney, Sydney, NSW 2006, Australia
*Corresponding author: dage@ece.umd.edu

Received 26 September 2018; accepted 2 November 2018; posted 15 November 2018 (Doc. ID 346720); published 12 December 2018

We present a silicon nitride/silicon dioxide add–drop filter operating on arbitrarily spaced channels using multimode interferometers (MMIs) and complex waveguide Bragg gratings (CWBGs). The add–drop filter shows a rejection ratio of >40 dB on all five channels, with a line width of 1.2 nm and an on-chip loss of <1 dB. By designing the CWBG with the Layer Peeling/Layer Adding algorithm, this MMI-CWBG add–drop filter platform has the capability for ultrabroadband add–drop operation on arbitrarily spaced channels.

https://doi.org/10.1364/OL.43.006045

On-chip optical filters have recently attracted great interest because they are the building blocks of integrated nanophotonic circuits. Multiple approaches have been proposed to realize on-chip optical filtering such as techniques based on arrayed waveguide gratings (AWG) [1] and echelle gratings [2]. However, in many applications, both transmitted and rejected signals are required. For example, in exoplanet detection, astronomers wish to separate the spectral components at certain wavelengths from the background and compare them to determine whether water and oxygen exist in the atmosphere of the observed exoplanet. While neither AWG or echelle gratings, nor many other on-chip multiplexing/demultiplexing techniques can separate and collect both transmitted and reflected signals simultaneously, on-chip add–drop filters provide a unique solution to this issue and also facilitate, for instance, the separation between a strong pump and weak idler and signal beam in quantum information applications [3], and new optical switches using thermal [4] or electrical tuning [5].

Many on-chip add–drop filters have been implemented with grating contradirectional couplers [6–8], phase-modulated shifted Bragg gratings [9–11], multimode interferometer (MMI) and and waveguide Bragg grating (WBG) systems [12–14], multimode antisymmetric WBGs [15], and ring resonators [16,17]. Among these techniques, WBG-MMI systems have demonstrated a highly flexible add–drop operation capability by changing the WBGs from simple Bragg gratings to gratings of different types, such as phase-shifted Bragg gratings and apodized Bragg gratings [12–14]. The operating principle of the WBG-MMI filter is shown in Fig. 1. Light injected into the input port is evenly split into two branches by the first 2 × 2 MMI, then both light beams are injected in the following identical WBGs. The transmitted signals from the two arms go to the through port after reflected signals converge on the drop port. The add port does not receive any light in this whole process, which minimizes the on-chip loss. In fact, this technique is particularly attractive because it can realize the add–drop operation with any type of WBG in between if the two WBGs are identical and their Bragg wavelength is located within the bandwidth of the MMI.

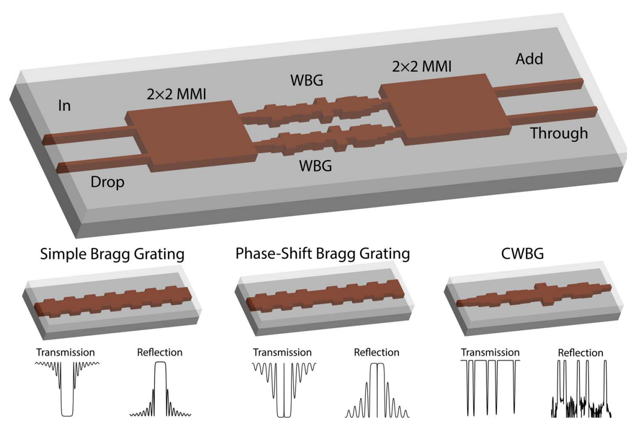

Fig. 1. Schematic layout of the WBG-MMI add–drop filter. Light injects from the input channel waveguide and is evenly split after the first 2 × 2 MMI. The transmitted light goes towards the through port after the second 2 × 2 MMI while the reflected light refocuses on the drop port. The WBGs between two MMIs can be of arbitrary types, i.e., simple Bragg grating, phase shift Bragg grating and complex waveguide Bragg grating, for different applications.

This flexibility enables us to extend the add–drop operation from single channel to multichannels when the WBG is designed to have multiple resonant wavelengths. By optimizing the design of the 2×2 MMI, the 3-dB bandwidth of WBG-MMI can be as broad as several hundred nanometers, thus making the WBG-MMI promising for ultrabroadband multiwavelength add–drop operation.

In this Letter, we first optimize the MMI design to maximize its 3-dB bandwidth for ultrabroadband add–drop operation. Then we fabricate a silicon nitride/silicon dioxide WBG-MMI add–drop filter with simple Bragg grating to demonstrate the robustness of this WBG-MMI platform. The silicon nitride/silicon dioxide system has been shown to be an ultralow loss and is transparent from visible to midinfrared range [18,19]. Finally, by substituting the simple WBG with the complex waveguide Bragg grating (CWBG), we demonstrate a CWBG-MMI add–drop filter with five channels at arbitrary preselected wavelengths. Carefully designed with the layer peeling/layer adding (LP/LA) algorithm, the CWBG exhibits a great potential to operate on more channels with narrower line widths.

MMI works based on the "self-imaging" principle [20]. Light entering the multimode propagation region excites modes of different orders that are supported in the multimode waveguide. Along the propagation direction, these modes interfere with each other, and a different number of images of the input optical field can be obtained at different propagation lengths.

In our add–drop filter application, because we need to separate the transmitted and reflected light signal from gratings, we design a 2×2 MMI that can divide the incoming optical power from one of the input ports equally into two output branches with a $\pi/2$ phase shift between the two output channels. This power uniformity plays an important role in the final extinction ratio between the through and add ports.

There are several design parameters. First, a better power uniformity is achieved when a larger number of modes is supported in the multimode region. Therefore, a wider multimode section is desired. However, on the other hand, the larger the width difference between the multimode waveguide and the access waveguide (which is fixed to satisfy the single-mode condition), the more the power is radiated away at their junctions because of the width mismatch. A second parameter is the offset of ports from the center of the multimode waveguide. If the two output ports are already sufficiently separated from each other, there is no need to add bends to further increase their separation (to eliminate the directional coupling between the two subsequent Bragg gratings). But then it is usually the case that the MMI will not be working in the "paired interference" [20] mode, thus tripling the length of the multimode region, making the device unnecessarily large and degrading the bandwidth performance.

We set the width to be 28 μm, supporting 13 guided modes. For the 28 μm wide multimode waveguide, the spacing between the two output ports is 9.7 μm, which is not enough to completely avoid the mutual coupling. Thus, additional bends are added to widen this spacing further to 19.7 μm. A simulation using a commercial software FIMMWAVE gives 47.27% and 48.91% of input power received at the two output ports. As for the second issue, we implement two 2×2 MMIs with different offsets, satisfying different interference conditions, and we compare their 3-dB bandwidths.

Measured results are shown in Fig. 2. Clearly, the device working in the paired interference mode exhibits a much better bandwidth performance. We adopt this design in the following WBG-MMI and CWBG-MMI add–drop filter because it enables our filter to operate with an ultrabroadband add–drop operation.

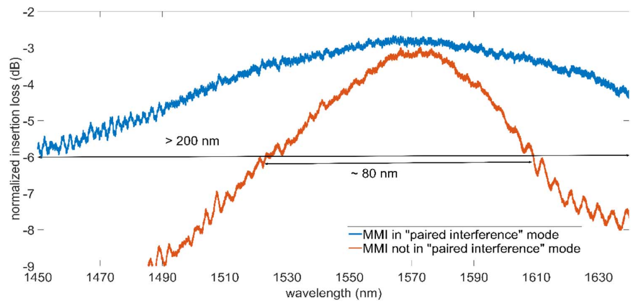

Fig. 2. Comparison of the bandwidth performance of the two implemented MMIs, with the power normalized to the input power. The one satisfying the paired interference condition shows a 3-dB bandwidth of more than 200 nm, while the other one is only 80 nm.

We then design a WBG-MMI add–drop filter with simple Bragg grating to validate its feasibility for add–drop operation. The Bragg grating is designed using a quarter-wave-stack, and it is centered at 1550 nm with a bandwidth of 10 nm. The length of the uniform Bragg grating in WBG-MMI is approximately 400 μm, and the coupling coefficient is about 80 cm^{-1}. 800 grating periods ensure a reflection ratio of ~57 dB at the Bragg wavelength. To characterize the add–drop filter, a TE-polarized tunable laser beam is launched into a polarization maintaining (PM) fiber and then coupled into the chip with a carefully designed high efficiency coupling taper [21]. After propagating through the sample, the light is again coupled out to a PM fiber and is analyzed by a power meter. The measured result of this WBG-MMI add–drop filter is shown in Fig. 3, with all linear propagation losses and fiber-taper coupling losses removed by normalizing the result to a reference waveguide. The center wavelength and the bandwidth of the implemented Bragg grating are 1558 and 8 nm, respectively. The discrepancy of the center wavelength between the simulation and measurement results is mainly attributed to the material refractive index difference between experiment and simulation, which could be corrected by adjusting the index used in the simulation. The on-chip losses of through and drop signals are less than 1 dB. The rejection ratio within the grating stop band is more than 50 dB. The in-add transmission is more than 25 dB lower than the in-through transmission, meaning that more than 99.5% of the transmitted light is refocused on the through port, thus contributing to the ultralow on-chip

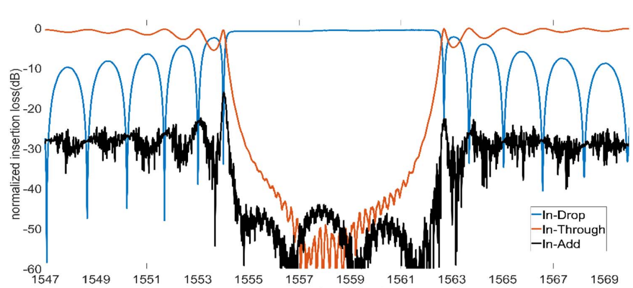

Fig. 3. Transmission and reflection signals of the WBG-MMI add–drop filter.

loss. Clearly, all these features prove the effectiveness of the WBG-MMI add–drop filter platform.

Finally, we replace the WBG with a CWBG to implement the arbitrary multichannel add–drop operation. The CWBG is designed with the LP/LA algorithm. The detailed description of the LP/LA algorithm can be found in [22,23]. As a summary, the LP/LA algorithm is based on Eqs. (1)–(3), where z is the grating position, δ is the wavenumber detuning from the central wavelength, ρ is the complex reflection coefficient, Δ is the layer peeling segment length, and $r(z, \delta)$ is the reflectivity at the z position with δ detuning, which contains wavelength information. When given the target reflection spectrum, we know $r(0, \delta)$, $\rho(0)$, and $r(\Delta, \delta)$ can be calculated from Eq. (1). Because in a real simulation the spectrum information must be discrete, we can convert continuous $r(\delta)$ to discrete $r(m)$ and calculate ρ in the next segment with Eq. (3). By iterating through this process, we can obtain ρ along the whole grating. We can also reconstruct $r(0, \delta)$, the target reflection spectrum, which is called the layer-adding process, with the layer peeling calculated $r(L, \delta)$ by using Eq. (2) to verify the correctness of the simulation. Finally, we map the complex reflection coefficient $\rho(z)$ to the physical width $w(z)$ of the CWBG and build the physical CWBG structure. It is notable that theoretically the target spectrum in the LP/LA algorithm can include any amount of dips with arbitrary positions, line widths, and rejection ratios. This is fundamentally different from other filtering techniques, such as the one based on ring resonators, which can only generate periodic reflection patterns. Our CWBG maximizes the flexibility of filter design and has already shown usefulness in applications requiring arbitrary light filtering such as OH-line suppression in the atmosphere for astronomy applications [24,25].

$$r(z+\Delta, \delta) = \exp(-i2\delta\Delta)\frac{r(z, \delta) - \rho(z)}{1 - \rho^*(z) r(z, \delta)}, \quad (1)$$

$$r(z, \delta) = \frac{r(z+\Delta, \delta) + \rho(z)\exp(-i2\delta\Delta)}{\exp(-i2\delta\Delta) + \rho^*(z) r(z+\Delta, \delta)}, \quad (2)$$

$$\rho(z) = \frac{1}{M}\sum_{m=1}^{M} r(m). \quad (3)$$

As a demonstration of the CWBG-MMI add–drop filter, we design a CWBG with five channels centered at 1550, 1554, 1563, 1569, and 1581 nm, respectively, which is aperiodic. Each channel has a rejection ratio of 65 dB and a 3-dB linewidth of 1.4 nm. The length of the CWBG is 5 mm, and the widths of the different segments varies from 1.4 to 2.9 μm, and correspond to a coupling strength κ that varies from 0 to 160 cm^{-1}. The discretization length of each segment in our CWBG is 4 nm.

The fabrication of the CWBG-MMI add–drop filter starts from a silicon wafer with 10 μm thermal grown silicon oxide. 100-nm-thick silicon nitride is deposited as the waveguide core using low-pressure chemical vapor deposition (LPCVD) techniques. Then, the CWBG-MMI add–drop filter is patterned by e-beam lithography with ZEP-520A, a positive tone resist. Next, chromium is deposited on the chip as the etching mask, followed by a lift-off process. After the inductively coupled plasma (ICP) etching of 100 nm, the silicon nitride core is covered with 6 μm silicon oxide, deposited by plasma-enhanced chemical vapor deposition (PECVD), as the cladding layer. Finally, the sample is cleaved for fiber-chip coupling. Scanning electron microscope (SEM) images are shown in Fig. 4. The two CWBGs between the two MMIs are identical and are only 19.7 μm apart, which contributes to its relatively small footprint. The zoomed-in SEM images shows that features as small as 100 nm are precisely defined and etched by e-beam lithography and ICP etching, both of which are critical for low loss and accurate CWBG filters.

Figure 5 shows the experimental result of the CWBG-MMI add–drop filter. The on-chip losses of both the transmission and reflection spectra are less than 1 dB from 1551 nm to more than 1590 nm. The total fiber-to-fiber loss of the CWBG-MMI is <9.5 dB. We expect to improve the throughput to <5 dB by optimizing the coupling taper. All five channels have rejection ratios of more than 40 dB and 3-dB bandwidth of 1.2 nm. The positions of the five channels are at 1549.40, 1553.40, 1562.27, 1568.28, and 1580.07 nm, respectively. Compared with the simulation result, the actual locations are blue-shifted by 0.73 nm. This is again mainly attributed to the material index difference between simulation and experiment, although we have already corrected the index used in the simulation based on the previous result of the WBG-MMI filter. This could be further improved by carefully measuring the refractive index of silicon nitride and silicon oxide. By aligning the position of the third channel in simulation and experimental results, we find that the precision of the channel spacing is better than ±0.2 nm. We also notice that the reflectivity at each channel is lower and the bandwidth is narrower than the design. In the simulation, we assume that the mode can fully react to the index variation whenever the width is changed. However, in the experiment, the mode travels to the next segment before it is fully coupled to the eigenmode of the current segment. Hence, the actual coupling strength

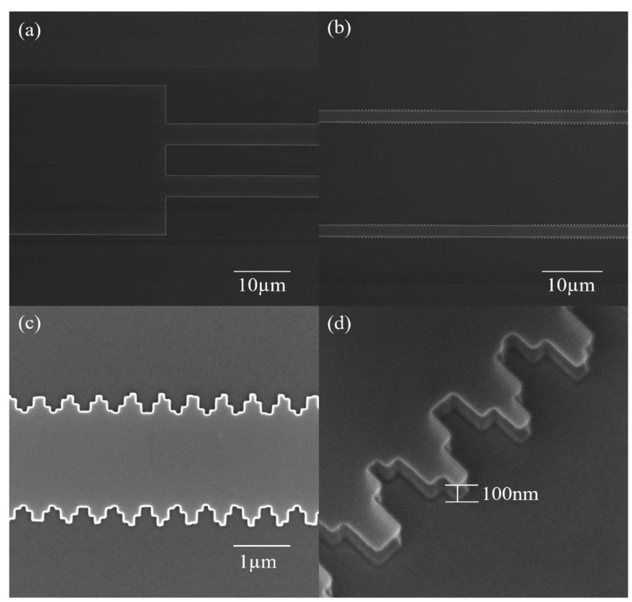

Fig. 4. SEM Images of the CWBG-MMI add–drop filter. (a) The MMI and its output waveguides. (b) Identical CWBGs in two arms. The designed CWBG is highly aperiodic. (c) Zoomed-in image of one of the CWBGs showing the precise definition of tiny structures with e-beam lithography. (d) 45° tilted view of the CWBG before final PECVD deposition. A smooth sidewall is achieved with the dry-etching process.

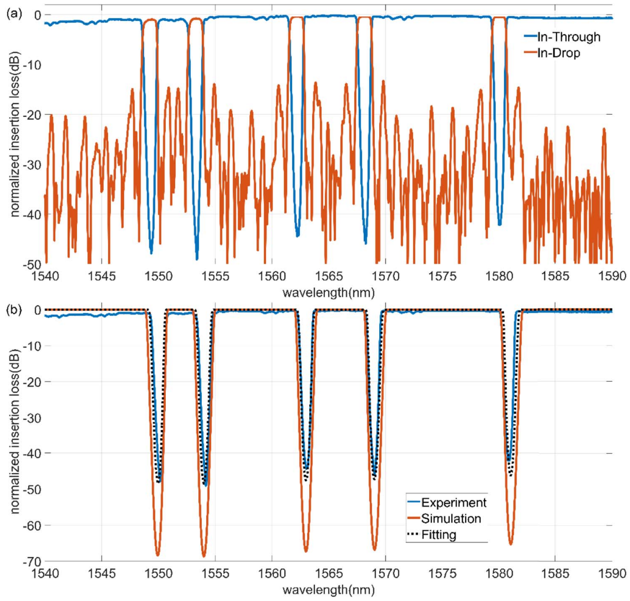

Fig. 5. (a) Experimental result of the transmission (blue line) and reflection (red line) spectrum. All five channels show an on-chip loss of <1 dB, a blue shift of 0.73 nm of center wavelengths, a spectral precision of better than ±0.2 nm, a rejection ratio of >40 dB, and a 3-dB bandwidth of 1.2 nm. (b) Comparison between the initial simulation result, the experimental result, and the fitted simulation result. The experimental result is red shifted by 0.73 nm to compensate for the mismatch of the positions of center wavelengths due to the index variation.

of the CWBG is weaker than that in the design. According to the Bragg grating theory, the grating bandwidth is related to the coupling strength κ (which is proportional to ρ in the LP/LA algorithm) and the reflectivity is related to κL. A weaker κ results in a shallower and narrower stop band. As shown in Fig. 5(b), the simulation shows that by changing the coupling strength κ to 0.73 κ_{LP} (LP calculated κ), the simulation result fits perfectly with the experimental result.

The results of both the CWBG-MMI and the previous WBG-MMI filters confirm that the WBG-MMI platform is robust and promising for ultralow loss, ultrabroadband and spectral-accurate add–drop operation. Because the MMI has a 3-dB bandwidth of more than 200 nm, the CWBG-MMI filter can potentially work over this whole wavelength range. By increasing the length of the CWBG and reducing the index variation, more reflection lines can be added into the spectrum with narrower line widths, while maintaining the high channel rejection ratio.

In conclusion, we have demonstrated the optimization of the design of a 2 × 2 MMI, a WBG-MMI add–drop filter with simple WBG, and a CWBG-MMI add–drop filter that has five arbitrarily spaced channels. The CWBG-MMI filter features an on-chip loss of <1 dB, a rejection ratio of >40 dB, a 3-dB line width of 1.2 nm, and a spectral precision of better than ±0.2 nm. To our knowledge, this is the first CWBG-MMI multichannel add–drop filter ever made. The LP/LA algorithm gives further flexibility to design filters with more notches with narrower line widths. The designed MMI ensures a large bandwidth of >200 nm for the proposed CWBG-MMI filter to work in. The CWBG-MMI platform provides a solution for ultrabroadband arbitrary-channel add–drop operation.

Funding. National Science Foundation (NSF) (AST-1711377, EFMA-1741651); Goddard Space Flight Center (GSFC) (APRA16-0064).

Acknowledgment. The authors thank the staff at the University of Maryland Nanocenter fabrication laboratory for their help with various fabrication techniques.

REFERENCES

1. P. Gatkine, S. Veilleux, Y. Hu, J. Bland-Hawthorn, and M. Dagenais, Opt. Express **25**, 17918 (2017).
2. C. Sciancalepore, R. J. Lycett, J. A. Dallery, S. Pauliac, K. Hassan, J. Harduin, H. Duprez, U. Weidenmueller, D. F. G. Gallagher, S. Menezo, and B. B. Bakir, IEEE Photon. Technol. Lett. **27**, 494 (2015).
3. N. C. Harris, D. Grassani, A. Simbula, M. Pant, M. Galli, T. Baehr-Jones, M. Hochberg, D. Englund, D. Bajoni, and C. Galland, Phys. Rev. X **4**, 041047 (2014).
4. R. Sumi, R. K. Gupta, N. DasGupta, and B. K. Das, IEEE J. Sel. Top. Quantum Electron. **25**, 8300111 (2018).
5. C. Errando-Herranz, F. Niklaus, G. Stemme, and K. B. Gylfason, Opt. Lett. **40**, 3556 (2015).
6. D. Charron, J. St-Yves, O. Jafari, S. LaRochelle, and W. Shi, Opt. Lett. **43**, 895 (2018).
7. H. Qiu, J. Jiang, P. Yu, D. Mu, J. Yang, X. Jiang, H. Yu, R. Cheng, and L. Chrostowski, J. Lightwave Technol. **36**, 3760 (2018).
8. B. Naghdi and L. R. Chen, IEEE Photon. J. **10**, 1 (2018).
9. S. Paul, T. Saastamoinen, S. Honkanen, M. Roussey, and M. Kuittinen, Opt. Lett. **42**, 4635 (2017).
10. S. Paul, M. Kuittinen, M. Roussey, and S. Honkanen, Opt. Lett. **43**, 3144 (2018).
11. S. Paul, I. Vartiainen, M. Roussey, T. Saastamoinen, J. Tervo, S. Honkanen, and M. Kuittinen, Opt. Express **24**, 26901 (2016).
12. A. D. Simard and S. LaRochelle, Opt. Express **23**, 16662 (2015).
13. J. Wang and L. R. Chen, Opt. Express **23**, 26450 (2015).
14. M. Caverley, X. Wang, K. Murray, N. A. Jaeger, and L. Chrostowski, IEEE Photon. Technol. Lett. **27**, 2331 (2015).
15. J. Jiang, H. Qiu, G. Wang, Y. Li, T. Dai, X. Wang, H. Yu, J. Yang, and X. Jiang, Opt. Express **26**, 559 (2018).
16. P. Rabiei, W. H. Steier, C. Zhang, and L. R. Dalton, J. Lightwave Technol. **20**, 1968 (2002).
17. K. Djordjev, S. Choi, S. Choi, and R. D. Dapkus, IEEE Photon. Technol. Lett. **14**, 828 (2002).
18. Y. Hu, Y. Zhang, P. Gatkine, J. Bland-Hawthorn, S. Veilleux, and M. Dagenais, IEEE J. Sel. Top. Quantum Electron. **24**, 1 (2018).
19. X. Ji, F. A. S. Barbosa, S. P. Roberts, A. Dutt, J. Cardenas, Y. Okawachi, A. Bryant, A. L. Gaeta, and M. Lipson, Optica **4**, 619 (2017).
20. L. B. Soldano and E. C. M. Pennings, J. Lightwave Technol. **13**, 615 (1995).
21. T. Zhu, Y. Hu, P. Gatkine, S. Veilleux, J. Bland-Hawthorn, and M. Dagenais, IEEE Photon. J. **8**, 7102112 (2016).
22. T. Zhu, Y. Hu, P. Gatkine, S. Veilleux, J. Bland-Hawthorn, and M. Dagenais, Appl. Phys. Lett. **108**, 101104 (2016).
23. J. Skaar, L. Wang, and T. Erdogan, IEEE J. Quantum Electron. **37**, 165 (2001).
24. J. Bland-Hawthorn, S. C. Ellis, S. G. Leon-Saval, R. Haynes, M. M. Roth, H.-G. Löhmannsröben, A. J. Horton, J.-G. Cuby, T. A. Birks, J. S. Lawrence, P. Gillingham, S. D. Ryder, and C. Trinh, Nat. Commun. **2**, 581 (2011).
25. C. Q. Trinh, S. C. Ellis, J. Bland-Hawthorn, J. S. Lawrence, A. J. Horton, S. G. Leon-Saval, K. Shortridge, J. Bryant, S. Case, M. Colless, W. Couch, K. Freeman, H.-G. Loehmannsroeben, L. Gers, K. Glazebrook, R. Haynes, S. Lee, J. O'Byrne, S. Miziarski, M. M. Roth, B. Schmidt, C. G. Tinney, and J. Zheng, Astron. J. **145**, 51 (2013).